Diabatic paths through the scission point in nuclear fission

G. F. Bertsch, W. Younes, and L. M. Robledo

Diabatic paths through the scission point in nuclear fission

G.F. Bertsch

Institute for Nuclear Theory and Department of Physics,
University of Washington, Seattle, Washington, USA[*]

W. Younes

Lawrence Livermore National Laboratory, Livermore, CA 94551, USA

L.M. Robledo

Departamento de Fisica Teorica, Universidad Autónoma de Madrid, E-28049 Madrid, Spain

An outstanding problem in the theory of nuclear fission is to understand the Hamiltonian dynamics at the scission point. In this work the fissioning nucleus is modeled in self-consistent mean-field theory as a set of Generator Coordinate (GCM) configurations passing through the scission point. In contrast to previous methods, the configurations are constructed in the Hartree-Fock approximation with axially symmetric mean fields and using the K-partition numbers as additional constraints. The goal of this work is to find paths through the scission point where the overlaps between neighboring configurations are large. A measure of distance along the path is proposed that is insensitive to the division of the path into short segments. For most of the tested K-partitions two shape degrees of freedom are adequate to define smooth paths. However, some of the configurations and candidate paths have sticking points where there are substantial changes in the many-body wave function, especially if quasiparticle excitations are present. The excitation energy deposited in fission fragments arising from thermal excitations in the pre-scission configurations is determined by tracking orbital occupation numbers along the scission paths. This allows us to assess the validity of the well-known scission-point statistical model, in which the scission process is assumed to be fully equilibrated up to the separated fission fragments. The nucleus ^{236}U is taken as a representative example in the calculations.

PACS numbers:

I.   INTRODUCTION

The final step of nuclear fission, namely the scission into two (or more) distinct fragments, has always been difficult to understand in fully microscopic models. In particular, self-consistent mean-field theory has been very successful in treating many aspects of fission theory but has shed little light on the final scission dynamics. The problem can be seen in typical constructions of fission paths by the Generator Coordinate Method (GCM) [1]. This involves a constrained minimization of the mean-field configurations, treating the expectation value of each constraining field as a coordinate. Most important among the coordinates is the elongation of the system. Configurations along the fission path are step-wise defined by re-minimizing the previous configuration at a slightly larger elongation, but more sophisticated propagation methods are possible [2–4]. At the scission point these procedures break down: the re-minimization produces a configuration very different from the previous one. Efforts to construct a continuous path have often focused on introducing more shape constraints, but the difficulties remain [5, 6].

In this work we will also follow the GCM approach, but with some differences from previous work. We will use the Hartree-Fock rather Hartree-Fock-Bogoliubov approximation to represent the configurations. We assume that the mean-field potential is axially symmetric, so the angular momentum of the orbitals about the fission axis K is conserved. Then the dynamics conserves the number of particles in orbitals of a given K. The set consisting of the number of occupied orbitals for each K will be called the *K-partition*. The resulting dynamics, preventing particles from jumping orbitals, is called[1] *diabatic* [10–12]. In Ref. [14] we have explored some of the diabatic configurations in ^{236}U leading to scission. In this work we study in more detail the changes in the wave functions and energies going through the scission point.

One may question whether the axially symmetric basis is adequate for representing configurations along the fission path. It is accepted wisdom that axial symmetry is broken at the first fission barrier and triaxial shapes should be taken into account for computing the barrier height[2]. But the computed shapes farther along the fission path are axially symmetric or nearly so. In particular, the mean-field shapes we found at the scission point have minima at axial symmetry.

---

[*]Electronic address: bertsch@uw.edu

---

[1] See Refs. [7–9] for examples of its application in other research fields.

[2] See [15] and references cited therein.

There are several characteristics of a diabatic path through scission that we will examine. The first is to determine the difficulty in defining a smooth path in terms of the number of shape constraints need. Our original hope was that a single elongation constraint would suffice, but that turns out not to be adequate. We also define and evaluation a measure of the length of the path through the scission point; long path are more difficult to traverse and the quantum theory would require more GCM configurations to describe them. An important physical question is how the scission dynamics affects the energies in the final state fragments. The configurations on the fission path are the lowest energy ones subject to the constraints, which we call the zero-quasiparticle configurations (ZQP). The excitation energy above the ZQP configuration can be affected by the scission in two ways. First, the diabatic dynamics could induce quasiparticle excitations, thereby increasing the total excitation energy in the final state. Even if this does not occur, the diabatic evolution will change the excitation energy because the quasiparticle energies will change. Also, the excitation energy sharing between fragments is determined at the scission point. In Sect. II below we take the example of the configuration named Glider in Ref. [14] to explain how we calculate the various properties of interest. An important question is how much of the behavior seen for Glider is generic with respect to different K-partitions or different energy functionals. In Sect. III we analyze several more K-partitions with two quite different energy functionals to see what general conclusions can be made. One particular question is how well statistical approaches to the scission dynamics can be justified in a microscopic approach. There has been considerable success of the scission-point statistical model [16–18] which assumes that the excitation energy is fully equilibrated between the two fragments at some fixed separation between their surfaces. In particular, Ref. [18] finds good agreement with experiments sensitive to the energy sharing.

II. GLIDER

We first summarize how the GCM scission configurations were constructed in Ref. [14]. The calculations are carried out[3] with the code HFBaxial [20] using the Gogny D1S energy functional [21]. The code finds minima in the Hartree-Fock-Bogoliubov energy functional constrained by the expectation values of external fields that serve as generator coordinates. The GCM fields available are the mass multipole moments[4]

$$\hat{Q}_L = r^L P_L(\cos\theta), \tag{1}$$

---

[3] See Supplementary Materials [19] for sample wave functions and the codes used to analyze them.
[4] Note that Q_2 defined here is one-half the conventional definition.

and fields associated with particle number and its fluctuations in the HFB wave functions. The code assumes that the single-particle Hamiltonian is axially symmetric. To find typical scission configurations, we constructed a fission path by HFB minimizations with only one shape constraint, namely the mass quadrupole moment Q_2. The minimizations were carried out iteratively starting from the ground-state configuration. At each cycle in the iteration, the Q_2 was increased by a small amount using the previous minimum as the starting configuration. For the nucleus ^{236}U, the configuration underwent a major rearrangement at $Q_2 \approx 168$ b. At that point the shape changed abruptly with a near disappearance of the neck joining the two proto-fragments. To get a closer view of the wave function dynamics at that point we determined the dominant Hartree-Fock configuration in the HFB wave functions. This was carried out by re-minimization of the HFB configuration with an added constraint on the number operator $\hat{N}^2$, effectively turning off the pairing field. Since the single-particle Hamiltonian is axially symmetric, the HF configurations can be characterized by its K-partition as well as by its density moments.

Among the HF states found, Glider is an intermediate configuration just at the edge of the scission point; its K-partition is given in Table I.

K-partition	protons						neutrons					
$2K$	1	3	5	7	9	11	1	3	5	7	9	11
Glider	22	14	6	3	1	0	31	20	11	6	3	1
A	22	14	7	3	0	0	31	21	12	6	2	0
B	21	13	7	4	1	0	30	20	11	7	3	1
C	21	14	7	3	1	0	30	21	11	6	3	1
C'	22	14	7	3	0	0	31	21	12	6	2	0

TABLE I: K-partition of the configuration Glider and others to be discussed in Sec. III. The entries are the number of occupied orbits of a given $K > 0$. The total number of particles of given $|K|$ is twice that.

From that point the HFB fission path jumps abruptly to a configuration of separated fragments with very different shapes. The HF reduction shows that this is accompanied by a major rearrangement of orbital occupancies. However, constraining the K-partition allows one to track Glider over a wide range of deformations going into post-scission shapes. Its energy as a function of deformation is shown in Fig. 1. One can see a transition at $Q_2 = 168 - 170$ b where the neck disappears. Interestingly, there are two local minima at $Q_2 = 168$ and 170 b in the HF energy surface when constrained only by the Q_2 moments. The higher energy configurations are obtained by stepping from smaller to larger Q_2 values, and the lower ones by stepping in the opposite direction. Beyond these two Q_2 points, the iteration gives identical configurations in both directions. The density distributions of the $Q_2 = 166$ b configuration $|166\rangle$ and the
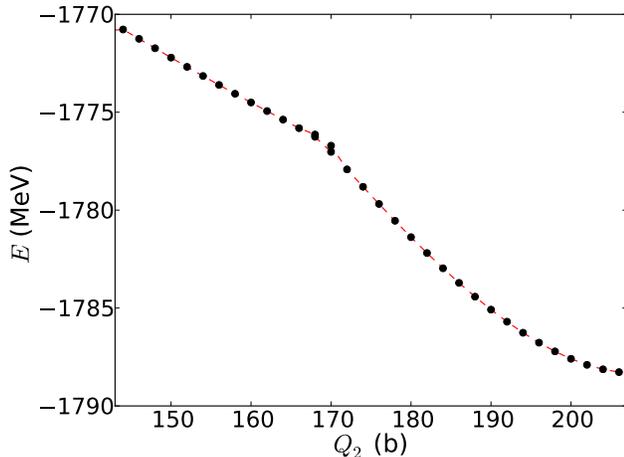
FIG. 1: Energy of Glider with the D1S energy functional and constrained by the quadrupole field Q_2.
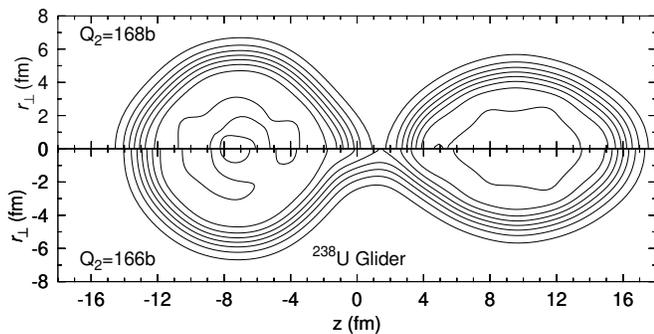

FIG. 2: Density distributions of the Glider configurations at two HF minima at the scission point. Top panel: configuration $|168p\rangle$; bottom panel: $|166\rangle$. Contour lines of the mass density are spaced by $\Delta\rho = 0.016$ fm^{-3}.
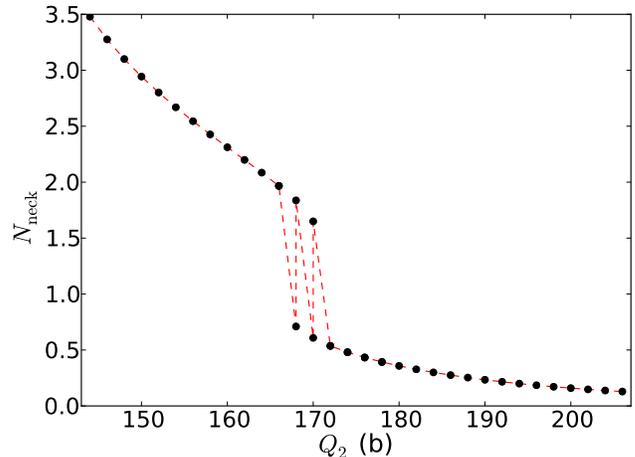

FIG. 3: Neck parameter N_{neck} as a function of deformation for Glider. The circles starting from the upper left are the HF minima constrained by Q_2 stepping from the previous solution at $Q_2 - 2$ b. The minima starting from the lower right are similarly constrained stepping from the previous solution at $Q_2 + 2$ b. There are two distinct minima at $Q_2 = 168$ and 170 b.

	$|166\rangle$	$|168p\rangle$	heavy	light
Z	92	92	52	40
N	144	144	84	60
E (MeV)	-1775.8	-1776.1		
Q_2 (b)	166	168	1.5	4.8
Q_3 (b$^{3/2}$)	50.2	51.4	0.06	0.06
N_{neck}	2.0	0.7		

TABLE II: Properties of the configuration Glider at the pre-scission point $Q_2 = 166$, and the post-scission solution at $Q_2 = 168$ b. The last two columns report properties of the daughter nuclei, extracted from the density distribution of the post-scission configuration at 168 b.

post-scission $Q_2 = 168$ b configuration $|168p\rangle$ are shown in Fig. 2. These configurations have a substantial overlap ($\langle 166|168p\rangle = 0.29$) and there is no obvious change in structure besides the disappearance of the neck. To analyze the transition in more detail, we will introduce an additional GCM coordinate based on a field sensitive to the number of nucleons in the neck region [22]. The definition is

$$\hat{N}_{\mathrm{neck}} = \exp\left(-(z - z_A)^2/a_N^2\right), \qquad (2)$$

with z_A chosen at the point along the fission axis z for which the density has a minimum, and $a_N = 1$ fm. Its expectation value as function of Q_2 is shown in Fig. 3. One sees that there is a discontinuous change in N_{neck} from ~ 1.7 to ~ 0.6 where there are two local minima. In Table II we show some of the characteristics of the two solutions. A continuous scission path can be constructed by adding $\hat{N}_{\mathrm{neck}}$ as a generator coordinate. For example, we can define a unique intermediate configura-

tion $|167m\rangle$ by constraining $Q_2 = 167$ b and $N_{\mathrm{neck}} = 1.1$, as both $|166\rangle$ and $|168p\rangle$ converge to it when the wave functions are re-minimized with the new constraint. The overlaps of the configurations are given in Table III. In

Overlaps	166	167m	168p
166	1.0	0.79	0.29
167m	0.79	1.0	0.67
168p	0.29	0.67	1.0

TABLE III: Overlaps of Glider configurations near the scission point.

principle, imposing a neck constraint will affect the mass split following scission. However, since we only impose the constraint when the neck is already formed, the effects will be small. We have checked that imposing the

neck constraint as we do does not change the mass split in the generated post-scission configurations.

It will be useful to have a cumulative measure of the overlaps along the scission path that is insensitive to the details of the step sizes used to construct the path. This is achieved by the distance function ζ defined as

$$\zeta = \sum_{n=1}^{N-1} \left(-\log |\langle n|n+1\rangle|\right)^{1/2}. \qquad (3)$$

for diabatic paths consisting of a chain of N configurations $|n\rangle$. Applying Eq. 3 to the path between end configurations in Table III, we find $\zeta = 1.13, 1.12$, and 1.13 with 0, 1, and 3 intermediate configurations. Clearly this satisfies our insensitivity demand.

A. Orbitals

Here we examine properties of the HF orbitals and how they evolve during the scission. An important goal is to calculate the changes in excitation energy associated with the scission and how that energy is distributed between the final state fragments. Up to now we have only treated ZQP configurations, but the theory can be easily extend by allowing partial occupation numbers n_α for orbitals α in the vicinity of the Fermi level. In the independent-quasiparticle approximation the excitation energy E^* above the ZQP value is given by

$$E^* = \sum_\alpha \varepsilon_\alpha \left(n_\alpha - n_\alpha^0\right) \qquad (4)$$

where $n_\alpha^0 = 0$ or 1 is the occupation number in the ZQP configuration. In the diabatic approximation, the orbital energies will change but the occupation factors will be frozen at the their initial values.

To calculate the sharing of excitation energy between the two fission fragments, we need to understand the localization of the orbitals onto one fragment or the other. A rough indicator the expectation value of the orbital density along the fission axis,

$$\langle z \rangle_\alpha = \int d^3r \, z |\phi_\alpha(\vec{r})|^2 \qquad (5)$$

Fig. 4 shows the orbital energies and their z-averaged positions for the configurations $|166\rangle$ and $|168p\rangle$, covering the energy band $-12 < \varepsilon - \varepsilon_f < 5$ Mev. The more deeply bound orbitals have $\langle z \rangle$ close to -7.3 or 9.6 fm, corresponding to the cm positions of the heavy or light fragment, respectively. For the post-scission configuration (upper panel of Fig. 4), practically all of the occupied orbitals follow that pattern. The situation is quite different for the pre-scission configuration shown in the lower panel. There are 10-20 orbitals that have much smaller $\langle z \rangle$, indicating a significant probability on both proto-fragments. One would expect that the extent of the bridging between the two fragments would depend
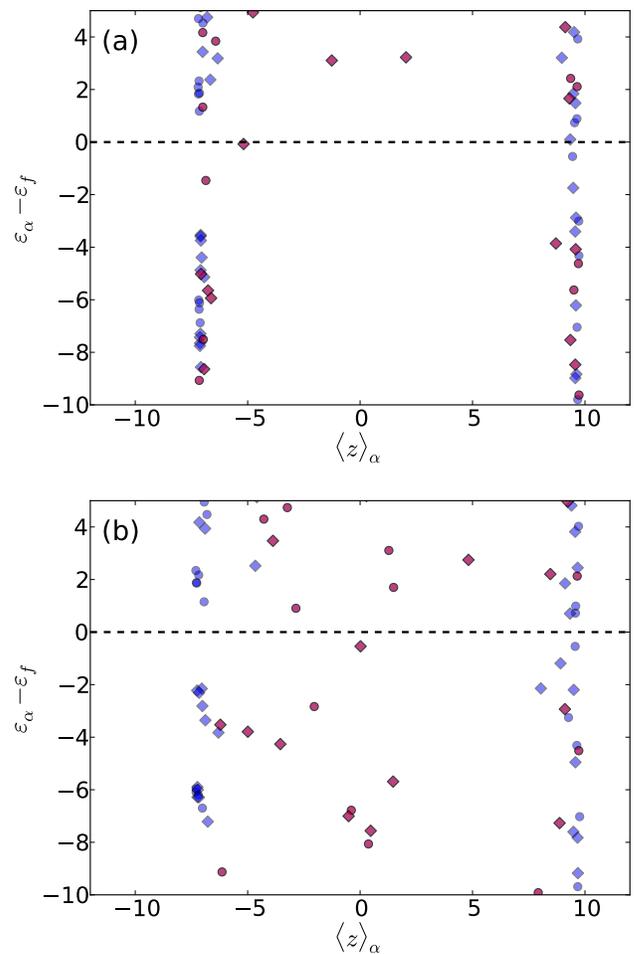

FIG. 4: Orbital locations and their energies as a function their expection value $\langle z \rangle_\alpha$. Panel (a): $|168p\rangle$; panel (b): $|166\rangle$. Proton and neutron orbitals are shown as circles and diamonds, respectively. The markers are red for $K = 1/2$ orbitals and otherwise blue.

strongly on K: orbitals with high K quantum numbers have small densities near the fission axis and would not have a substantial presence in the neck region. This is confirmed by the data shown in the Figure. One can see that most of the bridge orbitals have $K = 1/2$.

It is important for the diabatic treatment of the energy that the evolution of the orbitals can be tracked across the scission shape changes. This is hardly possible with the HFB wave functions constrained only by shape. With the HF wave functions and the two shape constraints Q_2 and N_{neck}, the orbitals evolve smoothly and one can identify the individual orbitals in the two end-point configurations with little ambiguity. This is illustrated in Fig. 5, showing how the orbital energies and their location vary as the neck size of the configuration decreases. For most of the orbitals (marked with 'A'), the absolute value of $\langle z \rangle$ increases as the neck becomes smaller. This is exactly what we expect: the bridge states straddling both proto-

fragments but become concentrated on one fragment or the other when the neck disappears. Orbitals that are already localized on one of the fragments (marked with 'B') hardly move at all. Interestingly, there are two orbitals that don't fit into the pattern. The orbitals near the 'C' marker move in the opposite direction. Undoubtedly, the reason is that there are two orbitals at nearly the same energy that mix together. When diagonal energies become degenerate, the mixing becomes maximal. This seems to occur in a configuration close to $|168p\rangle$. The orbital evolution marked with 'D' does not have any physical explanation. Perhaps the chain of orbitals was incorrectly assigned. Another feature seen in the bottom part of Fig. 5 is the effect of Coulomb repulsion when the neck becomes increasingly thinner: the repulsion between protons tend to remove proton orbitals off the neck region while those of neutrons progress more or less randomly.

B. Excitation energy

In principle there are three contributions to the energy of the pre-scission configurations. The first is the ZQP energy depending only on the shape parameters and the K-partition. The second contribution is the excitation energy associated with quasiparticle excitations. In this work we assume that it can be computed from the difference in the single-particle energies ε_α of the ZQP configuration. The last contribution, the collective kinetic energy, will not be treated explicitly in our work here.

We relate the excitation energy of the configuration to its quasiparticle spectrum using the standard grand canonical ensemble for occupation numbers n_α,

$$n_\alpha = \frac{1}{1 + \exp\left((\varepsilon_\alpha - \mu)/T\right)}. \tag{6}$$

Here μ is the chemical potential and T plays a role like temperature. The qualification "plays a role" is needed because a true temperature is a property of a fully equilibrated system rather than a system constrained by a specific K-partition. The T in the above equation is only used to relate the partial occupation probabilities to the total excitation energy. It is also important that μ be adjusted to give the correct average particle number in the ensemble.

We will calculate total excitation energies with using single-particle energies from both pre-scission and post-scission configurations $|166\rangle$ and $|168p\rangle$. We separate the orbitals into two sets, H and L depending on the orbital's location as indicated by $\langle z \rangle_\alpha$. For the pre-scission configuration, the orbital occupation numbers and single-particle energies are denoted by a superscript $(^-)$ as n_α^- and ε_α^-, and similarly with $(^+)$ for the post-scission orbitals. The excitation energy of the pre-scission configuration is given by Eq. (4) with $n_\alpha = n_\alpha^-$. We make a preliminary division between the two nascent fragments
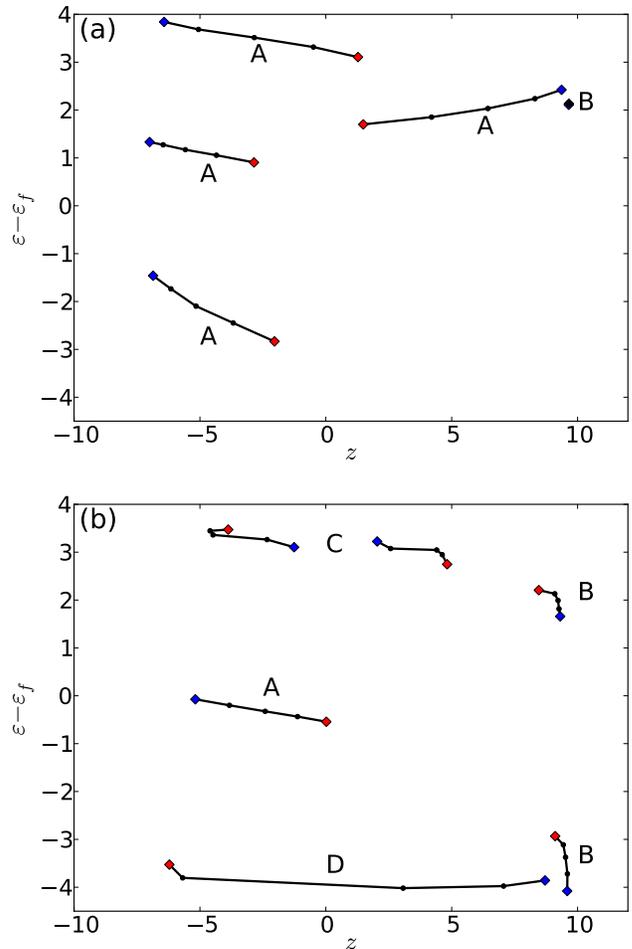

FIG. 5: $K = 1/2$ orbital energies and location parameters $\langle z \rangle$ as the Glider neck parameter changes. Panels (a) and (b) show proton and neutron orbitals respectively, for $|\varepsilon - \varepsilon_f| < 4$ MeV. Red diamonds: initial configuration $|166\rangle$; Blue diamonds: final configuration $|168p\rangle$. See text for comments on the marked orbitals.

from the energies

$$E_S^{*-} = \sum_{\alpha \in S} \left(n_\alpha^- - n_\alpha^{0-} \right) \varepsilon_\alpha^- \tag{7}$$

where S is the set H or L. This changes to

$$E_S^{*d} = \sum_{\alpha \in S} \left(n_\alpha^- - n_\alpha^{0+} \right) \varepsilon_\alpha^+ \tag{8}$$

after scission. Here the orbital occupation numbers are taken from pre-scission occupation factors but the quasiparticle energies from the post-scission configuration. As mentioned earlier, Eq. (8) requires tracking individual orbitals along the scission path. We saw in the last section that this can be carried out fairly confidently, at least for the orbitals near the Fermi energy. More details of how we link the pre-scission and post-scission orbitals

are given in the Appendix. For Glider orbitals, our procedure satisfies the check $n_\alpha^{0+} = n_\alpha^{0-}$ required for a ZQP diabatic path.

Table IV shows the energy partition calculated by the above equations for $|166\rangle$ and $|168p\rangle$ at initial excitation energies of 10 and 20 MeV. For each set of orbital energies, the parameter T in Eq. (4) is chosen to reproduce a given total E^*. The orbitals are assigned to H or L sets according to the sign of $\langle z \rangle_\alpha$. The average number of quasiparticles is given as N_{qp} in the Table. The final column in the table is the fraction of excitation energy in the heavy fragment,

$$f_H = \frac{E_H^*}{E^*}. \qquad (9)$$

The first point to notice is that the excitation energy hardly changes during the diabatic evolution. This is contrary to the expectation that diabatic transformations increase the internal energies of the system. Evidently this is not the case for Glider, which in fact evolves almost adiabatically within its K-partition constraint. However, we will see below an example of a diabatic evolution that explicitly injects excitation energy into the final state fragments.

Another important observable is the energy sharing between the post-scission fragments. We see from the Table that the quasiparticle excitation energy sharing is about the same in the pre-scission (Ensemble I) and post-scission (Ensemble II) states. To make contact with the scission-point statistical model, we also show energy sharing in an ensemble based entirely on the final state quasiparticle energy (Ensemble III). Here the occupation probabilities are computed with Eq. (4) without any K-dependent chemical potential. This ensemble shows some slight favoring of the lighter fragment. The computed energy fraction f_H is shown in the bottom entries to the Table. Experimentally, there is a strong favoring of the lighter fragment at this mass splitting. It is attributed to the proximity of the magic numbers 50 and 132 in the charge and mass numbers of the heavy fragment. Of course, our results should not be compared directly with experiment because the ZQP energy has not been included.

III. OTHER EXAMPLES

Glider is perhaps one of hundreds of configurations that can carry the ^{236}U nucleus past the scission point. Any general conclusions would require investigating a representative sample of them. Toward this end, we have found several other K-partitions that transition from shapes with distinct necks to separated fragments. Also, we present calculations with a different energy functional to get some indication of which qualitative features of the dynamics are generic or strongly functional-dependent.

Ensemble	T	N_{qp}	E^*	E_H^*	E_L^*	f_H
I	0.893	5.4	10.0	4.8	5.2	0.48
	1.164	8.7	20.0	10.4	9.6	0.52
II	0.896	5.4	10.1	5.4	4.6	0.54
	1.164	8.7	20.6	11.8	8.8	0.57
III	0.923	7.5	10.0	4.6	5.4	0.46
	1.21	10.7	20.0	9.8	10.2	0.49

TABLE IV: Thermal energy associated with Glider at the scission point. Ensemble I: Eq. (4) with $n_\alpha^-, \varepsilon_\alpha^-$ and preserving K-partition on average; Ensemble II: Eq. (8), diabatic with occupation numbers from I; Ensemble III: Eq. (4) with post-scission $n_\alpha^+, \varepsilon_\alpha^+$ and unrestricted by K-dependent chemical potentials. There are two rows for each method giving results for starting energies of 10 and 20 MeV. The third column is the number of quasiparticles $N_{qp} = \sum_\alpha |n_\alpha - n_\alpha^0|$. The last two entries are from a scission-point statistical model. The parameter T and excitation energies E^* are in units of MeV.

A. Other K-partitions

We consider here the three additional K-partitions labeled A,B,C in Table I. We have two measures of the dissimilarity of the configurations on either side of the scission. The first measure is the number of jumps in occupation numbers for the Q_2-constrained path through the scission region. In the case of Glider, there is a single jump down stepping from the left and a corresponding jump up stepping from the right; the two are very close in the Q_2 coordinate. These numbers are compared with the other configurations in Table V. The number

K-partition	Functional	N_j	Q_2	ζ
Glider	D1S	1	152-162	2.2
A	D1S	2	149	4.1
B	D1S	0	136	1.7
C	D1S	0	134	2.4
Glider	BCPM	2	156-175	2.6
A	BCPM	1	158	3.1
B	BCPM	1	141	1.7
C	BCPM	1	138	2.7

TABLE V: Characteristics of the GCM paths through the scission point. N_j is the number of jumps in N_{neck} going from pre-scission to post-scission shapes in steps of $\Delta Q_2 = 2$ b.

of downward jumps range from zero for K-partition B to two for A. Partition A is an especially difficult case for constructing a path through the scission point. Its energy as a function of the single Q_2 constraint is shown in Fig. 6. There are two configuration jumps stepping from smaller to larger Q_2, and one jump stepping from the other side, The coexistence of two configurations at the same Q_2 extends over a much larger range ($143 < Q_2 < 171$ b) than for the other cases. Add the
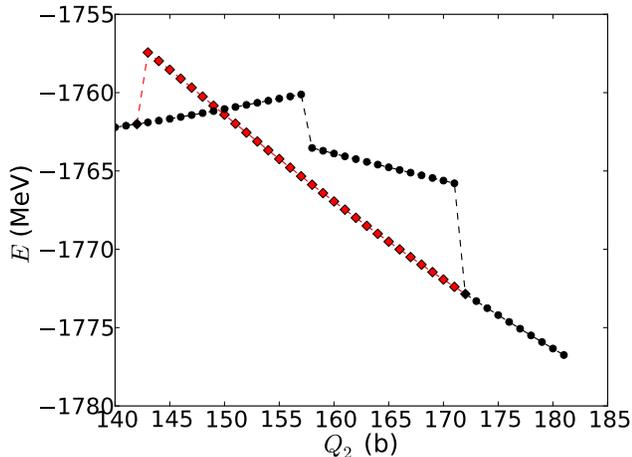
FIG. 6: Energy of the A configuration with the D1S energy functional and constrained by the quadrupole field Q_2. Black circles: iteration from the left; Red diamonds: iteration from the right.
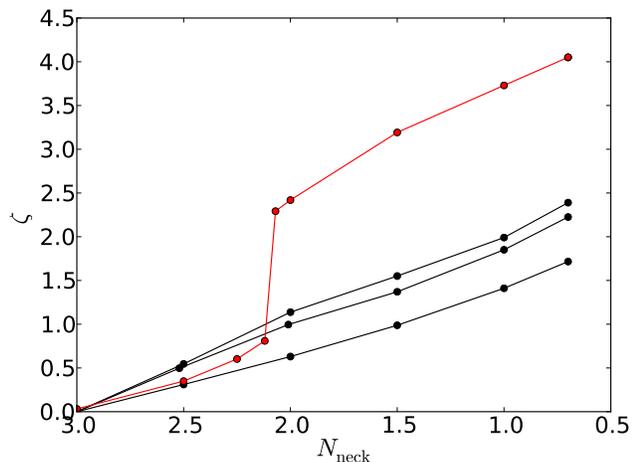

FIG. 7: Overlap distance ζ from $N_{\text{neck}} = 3.0$ to 0.7 for the four configurations Glider,A,B, and C with the D1S energy functional. The A configuration is distinguished by red lines and markers.

neck constraint brings the two paths close together but there remains a small region with two local minima.

Another measure of difficulty in traversing the scission point is the overlap distance ζ. Table V shows ζ for a path through the scission point defined by Q_2 and the neck size, with N_{neck} decreasing from 3.0 to 0.7. For most cases the distance is insensitive to the choice of Q_2. However, varying the Q_2 constraint along the path may make it somewhat shorter. To get a sense of the smoothness of the diabatic paths through the scission point we show ζ in Fig. 7 as a function of the neck constraint. One can see that partitions B and C are quite
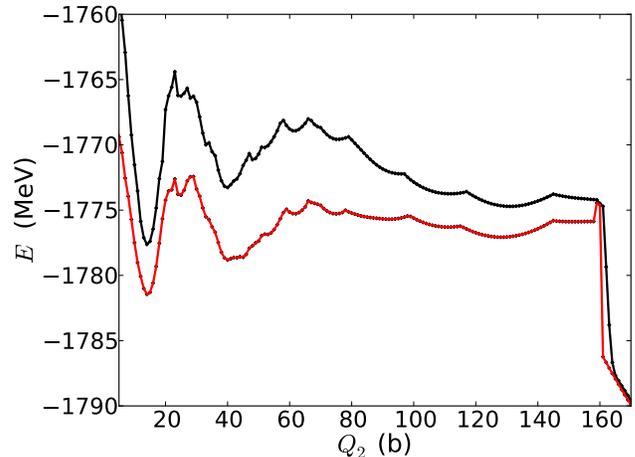

FIG. 8: Hartree-Fock potential energy surfaces for ^{236}U along the fission valley constrained by Q_2. The energies functionals are the D1S (black lines) and the BCPM (red lines). The cusps in the curves mark the positions where the orbital occupancies and K-partitions change. While the Q_2 is continuous by construction, the other moments of the shape distribution have discontinuities at these points. For example, the Q_3 moment jumps by ~ 2 b$^{3/2}$ at $Q_2 = 96$ b where a neutron pair in a $K = 3/2$ orbital jumps to a $K = 1/2$ orbital.

similar to Glider, but A has a major rearrangement at $(Q_2, N_{\text{neck}}) \approx (149 \text{ b}, 2.1)$. We have traced this behavior to the creation of a particle-hole excitation at this point in the path. A more detailed description is given in the Appendix.

B. The BCPM functional

We now carry out the same path analysis with the BCPM functional [23] which has been used in a previous fission study [24]. The single-particle potential in BCPM is purely local, giving a more realistic single-particle energy spectrum than the D1S. Despite the differences between the D1S and the BCPM, the fission paths along the valley bottom are very similar (Fig. 8). In particular, the sequence of K-partitions is identical starting from the ground state at $Q_2 = 14$ b to $Q_2 = 150$ b. However, closer to the scission point the paths are far from identical. Fig. 9 shows Glider's N_{neck} vs. Q_2 calculated as in Fig. 3, but using the BCPM functional. One sees that the region of ambiguity is larger and that there is a sudden jump from $N_{\text{neck}} = 1.8$ to 0.2 that is not present in the D1S trajectory. Numerical data about the paths for all the partitions treated in the last section are tabulated in the bottom rows of Table V. The N_j for BCPM are all different from the D1S values. Nevertheless the overlap distances through the scission point are within 0.4 units of each other, with the exception of partition A. Unlike the experience with D1S, the BCPM permits
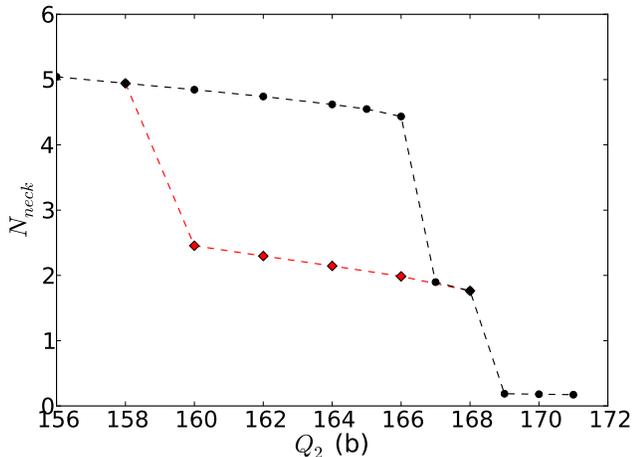
FIG. 9: Glider neck size with the BCPM energy functional and constrained by the quadrupole field Q_2. As in Fig. 6, iterations from the left and right are shown as black circles and red diamonds, respectively.
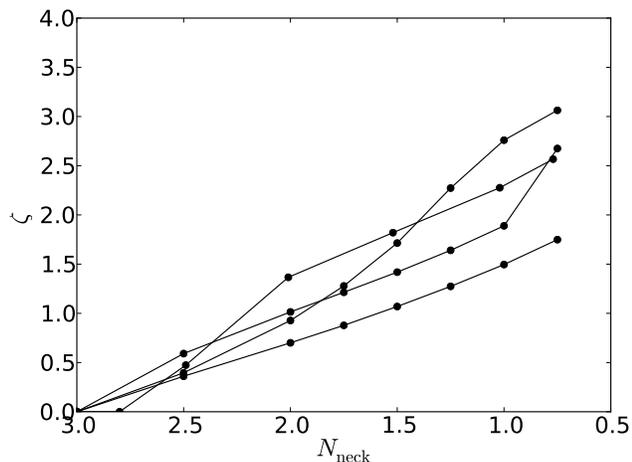

FIG. 10: Overlap distance ζ from $N_{\text{neck}} = 3.0$ to 0.7 for the four configurations Glider,A,B, and C calculated with the BCPM energy functional.

one to construct a path through the scission point with only two shape constraints. Fig. 10 shows ζ as function of N_{neck} as in Fig. 7. The curves look quite similar to the better-behaved D1S curves.

C. Excitation energies

As a final task to explore the sensitivities to input assumptions we repeat the calculation of excitation energy production and sharing during the scission. The results for all configurations and both energy functionals are shown in Table VI. The pre-scission and post-scission configurations are chosen at neck sizes $N_{\text{neck}} = 3.0$ and 0.7, respectively. The first thing to note is that the effective temperature is higher for the D1S functional than for the BCPM. This is not unexpected. Roughly speaking, the temperature associated with a given excitation energy depends quadratically on the effective mass in the energy functional. The BCPM has an effective mass of $m^*_{\text{bcpm}} = 1$ while the D1S has an effective mass of about $m^*_{\text{D1S}} = 0.67$. The average temperatures in the above Tables are 0.825 MeV and 0.728 MeV for BCPM and the square of their ratio is 0.7, rather close to $m^*_{\text{D1S}}/m^*_{\text{BCPM}}$.

Model	K-partition	T	f_H^-	f_H^d	E^{*d}
D1S	Glider	0.9	0.41	0.57	10.6
	A	0.86	0.31	0.35	18.9
	B	0.89	0.50	0.47	9.7
	C	0.85	0.50	0.39	8.6
BCPM	Glider	0.75	0.52	0.53	10.2
	A	0.695	0.29	0.39	11.9
	B	0.762	0.50	0.55	8.9
	C	0.705	0.54	0.50	4.9

TABLE VI: Fraction of excitation energy in the heavy fragment and total final state excitation energy for the diabatic evolution Details of the path constraints are given in Table V. The parameter T and excitation energies E^* are in units of MeV.

The excitation energies shown in the table and how they are shared between the fragments gives some idea of how much the scission-point dynamics affects these important quantities. Concerning the total excitation energy, the final diabatic excitation energy can be larger or smaller than the initial 10 MeV. Excluding partition A under D1S, the average change is -8%, largely driven by the 50% decrease in partition C under BCPM. The corresponding standard deviation of the energies is ±2 MeV. The other question is how the excitation energy get shared between the two fragments. For the 7 normal cases in Tables VI, the average fraction to the heavy fragment f_H and its standard deviation is 0.48 ± 0.07. The experimental f_H depends strongly on the mass splitting, and it can be reproduced in at least one version of the scission-point statistical model [18]. There they find $f_H \approx 0.36$ at $E^* = 10$ MeV; in our Table VI 3 out of the 8 partitions have energy fractions close to that value.

IV. CONCLUSION AND OUTLOOK

At the beginning of this study, we hoped that the constraint on K-partitions would be powerful enough to permit construction of paths through the scission point using a single shape constraint. This condition is met in two of the configurations, namely the ones that have no jumps in Table V. But typically two constraints are needed and

even that is inadequate for partition A under the D1S energy functional.

This makes it much harder to build a basis of configurations that could be treated with standard many-body techniques. Still, it is reasonable to assume the scission paths with short lengths (as measured by the overlap distance) will dominate in the decays. The more lengthy paths might be ignored in making first estimates of decay rates. It is intriguing to note that in the time-dependent approach to fission dynamics it has been found that there can be an important bottleneck at the scission point [25]. There it was found that the nucleus evolved smoothly to the scission point but remained there for a variable amount of time ranging up to $\tau_{\text{scission}} \approx 1.4 \times 10^4$ fm/c. This implies that the pre-scission configurations might have widths as small as $\Gamma \approx \hbar/\tau_{\text{scission}} \approx 10$ keV. Decay widths of the order 10 keV and higher would be consistent with the measured autocorrelation function for the $n+^{235}$U fission cross section, which does not show any systematic correlation on lower energy scales that could be attributed to the scission decay width [26].

As a next step in the present program, we would like to estimate Hamiltonian matrix elements between configurations along the scission path. In this respect, it will be quite helpful to be guided by the ζ distances when setting up the GCM space of intermediate configurations. It should then be possible to calculate decay widths of configurations near the scission point following the GCM methodology outlined in Ref. [27]. This could be carried out with the present computer codes, but it would be desirable to include collective momentum variables among the generator coordinates. Once one has the tools in place to calculate decay widths, it is a simple extension to the calculation of branching ratios by decay widths of different final states. For example, it would permit a fully microscopic theory of the distribution of kinetic energy in the final state (TKE).

In this study we have also used the diabatic paths to estimate the transport and changes in excitation energy across the scission point[5]. This is very relevant to the scission-point statistical model describing the distributions in mass yields and excitation energies of fission fragments. In that model, it is assumed that the scission itself has no dynamics role. This is belied by partition A which undergoes a 2-quasiparticle excitation on its scission path. However, this may be an anomalous case and it seems that ZQP paths are much more likely. For those paths, the average decrease is not much compared to all of the other uncertainties, and the variance is also small compared to other sources of fluctuation in the excitation energy. The conclusion is that ignoring diabatic dynamics remains an acceptable approximation in justifying the scission-point statistical model. However, no firm conclu-

---

[5] See Ref. [28] for another microscopic treatment of excitation energy transport.

sions can be drawn until a more representative sample of partitions can be examined.

Acknowledgment

V. APPENDIX

The possibility of creating particle-hole excitations along the fission path, and especially near scission, is of considerable interest in fission theory [29]. The excitation of intrinsic states in the latter stages of fission has a direct bearing on the excitation energy imparted to the fragments at scission, and the energy available for neutron emission. In this appendix, we discuss in more detail how we track the orbitals along the fission path by their overlaps, finding a particle-hole excitations on the diabatic path.

In a HF formulation of the problem, the orbitals are defined by the matrix W^q diagonalizing the single-particle mean-field Hamiltonian H^q. Here q are the constraints imposed in the minimization of the energy functional. The overlaps of orbitals α, α' at different q is simply the dot product of the two vectors

$$\langle \alpha q | \alpha' q' \rangle = \sum_i W_{i,\alpha}^{q*} W_{i,\alpha'}^{q'}. \tag{10}$$

As noted in section II, the calculations in this paper are carried out within the HFB framework, with the HF wave functions produced by constraining the pairing condensate to be small. In that case, the columns of the W matrix map into rows of the U matrix if the orbital is unoccupied and into rows of the V matrix if the orbital is occupied. Both cases are covered by the formula

$$\langle \alpha q | \alpha' q' \rangle = \sum_k \left[U_{\alpha k}^{q*} U_{\alpha' k}^{q'} + V_{\alpha k}^{q*} V_{\alpha' k}^{q'} \right] \tag{11}$$

when the occupation numbers are the same. If the occupation number changes, the nonzero amplitudes reside in the U matrix for one of the orbitals and in the V matrix for the other. Then the overlap may be computed as

$$\langle \alpha q | \alpha' q' \rangle = \sum_k \left[U_{\alpha k}^{q*} V_{\alpha' k}^{q'} - V_{\alpha k}^{q*} U_{\alpha' k}^{q'} \right]. \tag{12}$$
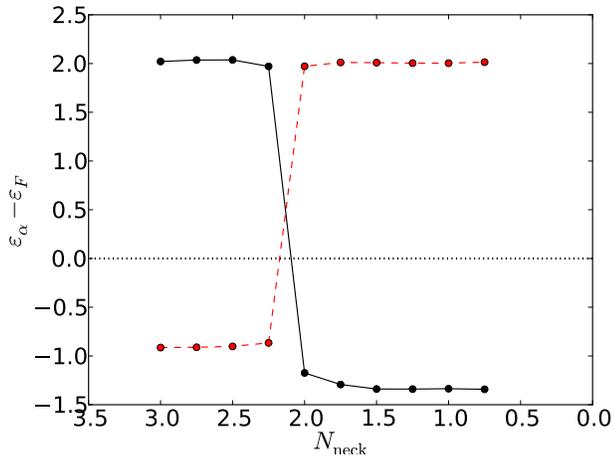
FIG. 11: Single-particle energies, relative to the Fermi energy, plotted as a function of neck size for the two lowest $K = 5/2$ proton orbitals for the configuration A at $Q_2 = 149\,$b. Energy units are MeV.

In practice, the larger in absolute value of Eqs. (11) and (12) is adopted as the optimal overlap. For each value of the K quantum number, the optimal overlaps $|\langle \alpha q | \alpha' q' \rangle|$ are calculated for all possible orbitals α, α'. The overlaps are then sorted from highest to lowest in absolute value. Proceeding down the list of sorted overlaps, the orbitals for the largest overlap are considered matched and taken out of consideration. The next largest overlap which does not involve those orbitals already taken out of consideration gives the next matched pair of levels. This process is repeated until all orbitals have been matched.

We now examine in detail the case where we found a possible particle-hole excitation, namely configuration A at $Q_2 = 149$ b in table V, calculated with the D1S interaction. The neck size was constrained from $N_{\rm neck} = 3$ down to 0.75 in steps of $\Delta N_{\rm neck} = 0.25$. After calculating orbital overlaps according to the above procedure, the first two proton orbitals in the $K = 5/2$ block were found to change occupations when going from $N_{\rm neck} = 2.25$ to 2. The tracked single-particle energies for those two orbitals are plotted as a function of neck size in Fig. 11. One orbital switches from occupied to unoccupied as the neck shrinks, while the other switches from unoccupied to occupied. This swap in occupation probabilities can be interpreted as a particle-hole excitation between the two configurations. Interestingly, both orbitals reside largely in the same fragment, but one has orbital angular momentum M nearly parallel to the spin angular momentum, $K = M + 1/2$ while the spin in the other is mostly antiparallel. The spatial densities of the orbitals in the HF representation are given by

$$\rho_\alpha (z) = \sum_{i,k} \delta_{K_i, K_k} \delta_{M_i, M_k} W^*_{i,\alpha} W_{k,\alpha} \qquad (13)$$
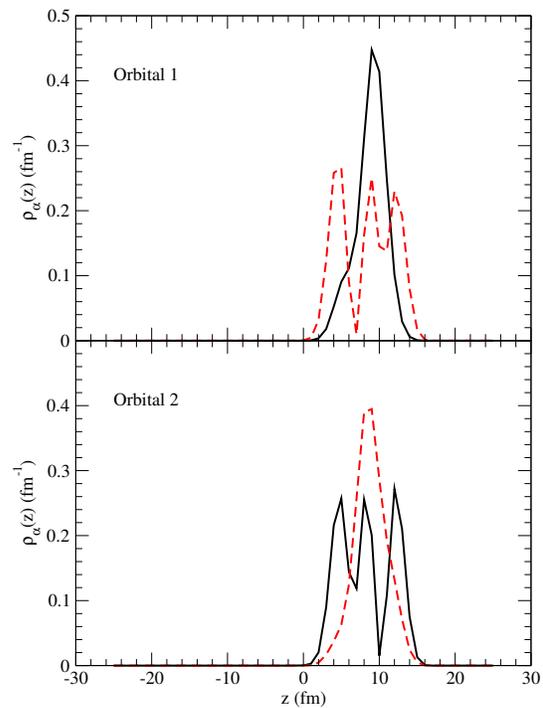

FIG. 12: Single-particle densities for the two $K = 5/2$ proton orbitals closest to the Fermi energy for the configuration A at $Q_2 = 149$ b Dashed red lines: $N_{\rm neck} = 2.00$; solid black lines: $N_{\rm neck} = 2.25$.

$$\times \int dx dy \; \phi_i^* (x, y, z) \phi_k (x, y, z)$$

where $\phi_k(\vec{r})$ are the basis orbitals. In the HFB representation we replace $W^*_{i,\alpha} W_{k,\alpha}$ in the above equation by $U^*_{\alpha,i} U_{\alpha,k} + V^*_{\alpha,i} V_{\alpha,k}$, similar to our treatment of Eq. (11).

The densities of the two $K = 5/2$ proton orbitals are shown in Fig. 12. The upper panel shows the densities in the orbital just below the Fermi level at $N_{\rm neck} = 2.10$ (dashed red line) and $N_{\rm neck} = 2.09$ (solid black line). The lower panel shows the corresponding densities of the orbital just above the Fermi level. It may be seen that the orbitals have very different spatial character: one has a single lobe centered near the middle of the fragment, while the other is extended over a much larger range of z and has three lobes.

The tracking results described above has an implicit dependence on the step size along the scission path. The diabatic evolution is (somewhat imprecisely) defined as the tracking with large step sizes as in Fig. 11. For small step sizes, one would expect an adiabatic evolution. That is, the orbitals will keep their position as ordered by their single-particle energies. The level crossings become avoided crossings, suppressing particle-hole excitations, except if prevented by symmetries. Indeed, we found this

to be the case here. The particle-hole transition takes place near $N_{\text{neck}} = 2.1$. We examine the orbital matched between two configurations around that point and separated by some ΔN_{neck}. For $\Delta N_{\text{neck}} \lesssim 0.07$, the overlaps in Eq. (11) are favored leading to a smooth transition across the critical neck size without p-h excitation. For $\Delta N_{\text{neck}} \gtrsim 0.07$, however, the overlaps in Eq. (12) are favored, resulting in a swap of occupation probabilities and a corresponding p-h excitation. Although the calculations in this paper are entirely static, the dependence on ΔN_{neck} mimics the range of dynamic evolution at scission, where smaller ΔN_{neck} values can be identified with

a slow process, and larger ΔN_{neck} values with a faster one.

However, there is one aspect of the Landau-Zener avoided-crossing picture in this example that remains a puzzle. Namely, the energies of the orbitals should smoothly pass by each other as a function of the shape parameter, except for a small region of the avoiding crossing. In fact, we find that the energies remain nearly constant along the scission path. Somehow, the wave functions are exchanged without the energies coming close together. Clearly, this aspect of the dynamics needs further study.

[1] M. Bender, P-H. Heenen and P-G. Reinhard, Rev. Mod. Phys. **75** 121 (2003).
[2] N. Schunck and L.M. Robledo, Rep. Prog. Phys. **79** 116301 (2016).
[3] D. Regnier, et al., Phys. Rev. C **93** 054611 (2016).
[4] J-F. Lemaitre, S. Goriely, S. Hilaire and N. Dubray, Phys. Rev. C **98** 024623 (2018).
[5] W.Younes and D. Gogny, Phys. Rev. C **80** 054313 (2009).
[6] N. Dubray and D. Regnier, Comp. Phys. Comm. **183** 2035 (2012).
[7] D. Yarkony, Chem. Rev. 112 481 (2012).
[8] T.Tamaya, et al., Phys. Rev. Lett. **116** 016601 (2016)>
[9] A. Scotti and P-Y. Passaggia, J. Fluid Mech. **861** 608 (2019).
[10] G. Schütte, Phys. Rep. **80** 113 (1981).
[11] W. Nörenberg, Nucl. Phys. A **409** 191c (1983).[A
[12] W. Nazarewicz, Nucl. Phys. A **557** 489 (1993).
[13] T. Nakatsukasa and N. Walet, Phys. Rev. C **58** 3397 (1998).
[14] G.F. Bertsch, W. Younes and L.M. Robledo, Phys. Rev. C **97** 064619 (2018).
[15] H. Abusara, A.V. Afanasjev and P. Ring, Phys. Rev. C **82** 044303 (2010).
[16] B.D. Wilkins, et al., Phys. Rev. C 14 1832 (1976).

[17] J.-F. Lemaitre, et al./ Phys. Rev. C **92** 034617 (2015).
[18] M. Albertsson, et al., arXiv:1811.02283 (2018)
[19] See Supplementary Material at [URL will be inserted by publisher] for data files corresponding to figures and tables and scripts to generate them.
[20] L.M. Robledo, unpublished. See [19] for the code HFBaxial.
[21] J.F. Berger, M. Girod and D. Gogny, Comp. Phys. Comm. 63 365 (1991).
[22] M. Warda, et al., Phys. Rev. C **66** 014310 (2002).
[23] M. Baldo, L.M. Robledo, P. Schuck, and X. Vinas, Phys. Rev. C **87** 064305 (2013).
[24] S. Giuliani and L.M. Robledo, Phys. Rev. C **88** 054325 (2013).
[25] A. Bulgac, P. Magierski, K. Roche and I. Stetcu, Phys. Rev. Lett. 116 063628 (2015).
[26] G.F. Bertsch, David Brown, and E.D. Davis, Phys. Rev. C **98**, 014611 (2018).
[27] G.F. Bertsch and W. Younes, Ann. Phys. **403** 68 (2019).
[28] Y. Tanimura, D. Lacroix, and S. Ayik, Phys. Rev. Lett. 118 152501 (2017).
[29] R. Bernard, H. Goutte, D. Gogny, and W. Younes, Phys. Rev. C 84, 044308 (2011).